

Haptics-Enabled Forceps with Multi-Modal Force Sensing: Towards Task-Autonomous Surgery

Tangyou Liu, Tinghua Zhang, Jay Katupitiya, Jiaole Wang*, *Member, IEEE* and Liao Wu*, *Member, IEEE*

Abstract—Many robotic surgical systems have been developed with micro-sized biopsy forceps for tissue manipulation. However, these systems often lack force sensing at the tool side. This paper presents a vision-based force sensing method for micro-sized biopsy forceps. A miniature sensing module adaptive to common biopsy forceps is proposed, consisting of a flexure, a camera, and a customised target. The deformation of the flexure is obtained by the camera estimating the pose variation of the top-mounted target. Then, the external force applied to the sensing module is calculated using the flexure’s displacement and stiffness matrix. Integrating the sensing module into the biopsy forceps, in conjunction with a single-axial force sensor at the proximal end, we equip the forceps with haptic sensing capabilities. Mathematical equations are derived to estimate the multi-modal force sensing of the haptics-enabled forceps, including pushing/pulling forces (Mode-I) and grasping forces (Mode-II). A series of experiments on phantoms and ex vivo tissues are conducted to verify the feasibility of the proposed design and method. Results indicate that the haptics-enabled forceps can achieve multi-modal force estimation effectively and potentially realize autonomous robotic tissue grasping procedures with controlled forces. A video demonstrating the experiments can be found at <https://youtu.be/JfLmSdaFufw>.

Index Terms—Surgical robotics, autonomous surgery, multi-modal force sensing, tissue manipulation.

I. INTRODUCTION

AN increasing number of robotic systems have been developed with miniature instruments to facilitate minimally invasive surgery (MIS) in the past decade [1], [2]. For example, micro-sized biopsy forceps have been widely adopted in recently developed robotic systems for tissue manipulation in narrow spaces [3]–[5]. However, one notable limitation of these systems is their lack of force sensing at the tool side for tissue manipulation, including pushing (Fig. 1(a)), grasping (Fig. 1(b)), and pulling (Fig. 1(c)) forces.

Force sensing for tissue manipulation is critically needed for two reasons. Firstly, information about these forces can enhance surgeons’ operation and decision-making if integrated into the systems appropriately [6]. For instance, Talasaz *et al.*

[7] verified that a haptics-enabled teleoperation system could perform better during a robot-assisted suturing task. Secondly, there is a consensus on the growth of autonomy in surgical robots [8] accompanied by more dexterous mechanisms such as snake-like robots [9], [10]. Force sensing at the tool side will play an essential role in the evolution of autonomous robotic surgery [8], [11].

Researchers have conducted various investigations to enable force sensing of different grippers for tissue manipulation. Zarrin *et al.* [12] fabricated a two-dimensional gripper that can measure grasping and axial forces with two Fiber Bragg grating (FBG) sensors embedded into the gripper’s jaws. Using the same principle, Lai *et al.* [13] developed a gripper that can estimate pulling and lateral forces. While these FBG-based designs usually present a high resolution of force detection, they always suffer from extreme sensitivity to temperature variation [14]. In addition, highly expensive interrogation systems are needed for these sensors to work. By integrating capacitance into a pair of surgical forceps’ two jaws, Kim *et al.* [15] enabled the forceps with multi-axis force sensing. However, the capacitance-based method is still susceptible to temperature changes [16]. Moreover, it is vulnerable to electromagnetic variation, which is inevitable when polarized instruments are adopted for tissue manipulation [17]. These limitations may invalidate the forceps’ force sensing capability when used in practical surgical tasks [18]. In addition, all the above methods require re-machining the forceps’ two jaws to install the proposed sensors, making them unsuitable for micro-sized biopsy forceps.

Recently, vision-based methods have also been explored for developing low-cost force sensors. Ouyang *et al.* [19] developed a multi-axis force sensor with a camera tracking a fiducial marker supported by four compression springs. The displacement of the marker was captured by the camera and converted to force information by multiplying a linear transformation matrix. Fernandez *et al.* [20] presented a vision-based force sensor for a humanoid robot’s fingers with almost the same principle. In addition to providing multi-dimensional force feedback, vision-based force sensing is relatively robust to magnetic, electrical, and temperature variations. However, these vision-based sensors developed so far are large in size and can only estimate contact forces that directly connect to the fiducial markers’ displacement.

Although vision has already been introduced into surgical systems, little work has investigated its force-sensing capability for surgical instruments. An exception is a visual-haptic module developed by Fagogenis *et al.* [21] for autonomous robotic intracardiac catheter navigation. The proposed module

Research was partly supported by Australian Research Council under Grant DP210100879 and Heart Foundation under Vanguard Grant 106988 awarded to Liao Wu, partly by the Science and Technology Innovation Committee of Shenzhen under Grant JCYJ20220818102408018 awarded to Jiaole Wang, and partly by the Tyree IHealthE PhD Top-Up Scholarship awarded to Tangyou Liu. *Corresponding authors: Jiaole Wang (wangjiaole@hit.edu.cn) and Liao Wu (liao.wu@unsw.edu.au).

Tangyou Liu, Jay Katupitiya, and Liao Wu are with the School of Mechanical & Manufacturing Engineering, The University of New South Wales, Sydney, NSW 2052, Australia.

Tinghua Zhang and Jiaole Wang are with the School of Mechanical Engineering and Automation, Harbin Institute of Technology, Shenzhen, 518055, China.

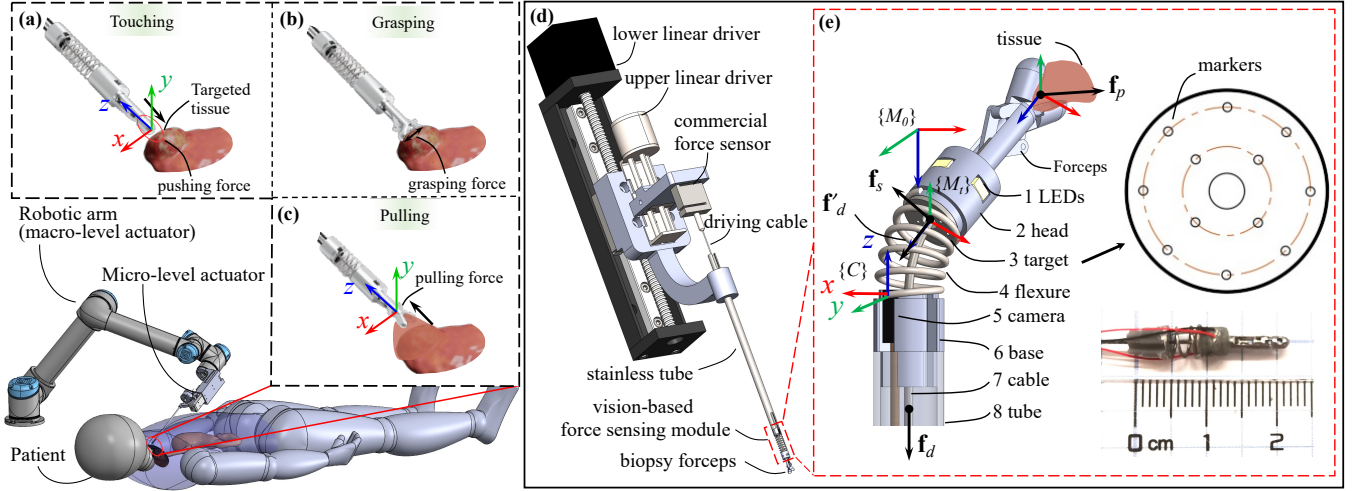


Fig. 1. Typical tissue manipulations using a pair of forceps in robotic thyroid tumour treatment, an example scenario of robotic surgery, and the critically required force information. (a) A pair of forceps touches the targeted tissue while measuring the pushing forces. (b) The forceps grasp the targeted tissue while measuring and controlling the grasping force. (c) The forceps pull the grasped tissue while measuring and controlling the pulling force. (d) The micro-level actuator used for driving the forceps, where a commercial single-axis force sensor measures the driving force applied to the forceps' driving cable. The upper and lower linear drivers are responsible for grasping and pushing/pulling, respectively. The lower driver also compensates for the motion introduced by the flexure's deformation when the upper driver grasps tissue. (e) The haptics-enabled biopsy forceps, where the forceps' base is concentrically installed to the vision-based sensing module's head (2). Two LEDs (1) are mounted in the sensing module's head (2) to provide light source in our prototype, which comes through the target's (3) holes and is captured by the camera (5) mounted on the other end of the flexure (4). The upper-right inset shows the installed target and the holes used as markers. The cylindrical base (6) provides a mount to connect to instruments, which is a stainless tube (8) in our prototype. Concentric to the module, a channel is reserved for the passage of the forceps' driving cable (7). The lower right inset shows a prototype that has a 4mm diameter and 22mm length. Plot (e) also shows the camera frame $\{C\}$, the target frames of the initial $\{M_0\}$ and current $\{M_t\}$ states, and the forces applied to the forceps when they push or pull the tissue. f_d is the driving force on the cable and is measured by the proximal commercial force sensor. f'_d is the driving force transmitted to the forceps' jaws through the central cable. f_s is the supporting force from the sensing module, and f_p is the pushing/pulling force from the tissue.

uses a camera to sense the contact between a silicone head mounted to the instrument's tip and the heart, according to the area and duration that the silicone head is covered by the tissues. However, it cannot be used to measure either the pushing/pulling force or the grasping force of forceps as it relies on the contact between the silicone head and the surrounding tissues.

In summary, despite many achievements for gripper force sensing based on various principles in the past few years, force estimation of micro-sized biopsy forceps for MIS, especially their grasping and pulling force measurement, is still challenging. This paper proposes a method to enable multi-modal force sensing of the widely adopted micro-sized biopsy forceps by combining a three-dimensional vision-based force sensing module at the tool side and a single-axis commercial strain gauge sensor at the proximal side, as shown in Fig. 1(d). The developed sensing module that can be easily integrated at the tool side is responsible for perceiving the interaction between the forceps and the manipulated tissues (Fig. 1(e)). The commercial strain gauge sensor mounted at the proximal side measures the force applied to the forceps' driving cable. By integrating these pieces of sensed information, mathematical equations are derived to estimate the forceps' touching, grasping, and pulling forces.

The main contributions of this article are two-fold:

- 1) A vision-based force-sensing module that can be easily integrated into micro-sized biopsy forceps is developed. An algorithm is designed to calculate the force applied to the sensing module with a registration method for

tracking and estimating the pose of the sensing module's target.

- 2) A design of haptics-enabled forceps is further proposed by assembling the widely used biopsy forceps with the developed sensing module embedded at the tool end and a single-axis strain gauge sensor mounted at the proximal end. Mathematical formulae are derived to estimate the multi-modal force sensing of the haptics-enabled forceps, including pushing/pulling force (Mode-I) and grasping force (Mode-II).

These contributions are validated by various carefully designed experiments on phantoms and ex vivo tissues. Results indicate that the haptics-enabled forceps can achieve multi-modal force estimation effectively and potentially realize autonomous robotic tissue grasping procedures with controlled forces.

II. HAPTICS-ENABLED BIOPSY FORCEPS

A. Design of A Vision-Based Force Sensing Module

1) *Overall Structure:* The design of the sensing module (Fig. 1(e)) has followed two requirements: 1) small in size, 2) adaptive to biopsy forceps. The module is designed in a cylindrical shape to minimize anisotropy, and the main components are a flexure, a camera, and a target. A central channel is reserved for the passage of instruments. The target, supported by the flexure, is manufactured with multiple holes that allow light to pass from a light source, and these holes can then be captured by a camera as markers for the estimation of the target's pose, as depicted in Fig. 1(e). The module's size

and stiffness can be customized based on the instruments' and applications' needs. Here, we assemble a prototype with a diameter of 4mm and a length of 12mm and integrate it in a pair of biopsy forceps, as shown in the lower-right of Fig. 1(e).

2) *Flexure*: Material properties and geometry play a dominant role in the multidimensional stiffness of the flexure. Different approaches have been adopted for flexure design, including the pseudo-rigid-body replacement method [22], topology optimization [23], etc. For force sensing in different surgical tissue manipulations, the flexure should also be changeable according to the task requirements. One commercial and readily available flexure is the compression spring [19], [20]. Although compression springs typically show dominant stiffness in the axial direction, they also exhibit a certain degree of stiffness in lateral directions and can be linearly approximated [24]. Moreover, they can be easily reconfigured by choosing different wire diameters, outer diameters, and coil numbers. For the prototype, we chose a stainless steel compression spring with a wire diameter of 0.5mm, outer diameter of 4mm, rest length of 5mm, and four coils. The selected spring has a force response range of 0~5N and 0~2N at axial and lateral displacements of 0~2mm and 0~1mm, respectively, which can meet the requirement of most tissue manipulations [25].

3) *Camera and Target*: The camera for the sensing module should have a compact size, sufficient resolution, and surgery compatibility. For the prototype, we chose OVM6946 (Ominivision Inc., USA), which has been adopted in many surgical applications [5], [26]. It is 1mm in width and 2.27mm in length and has a 400×400 resolution and 30Hz rate. To ensure continuous tracking and estimation, we fabricated the target with twelve cycle-distributed 0.15mm-diameter holes used as markers for the camera to track and estimate the target pose, and a central hole is reserved for tools to pass through. These holes can also be customized based on the instruments and applications. Considering the integration into the biopsy forceps for MIS, the prototype's target in Fig. 1(e) has a 3.4mm outer diameter and a 0.6mm-diameter central hole for the driving cable.

B. Force Estimation of Sensing Module

Ideally, for a linear-helix compression spring, the external force \mathbf{f}_s applied to the sensing module's head has an approximated relationship with the spring's displacement [24] as

$$\mathbf{f}_s = \mathbf{K}_s \mathbf{d}_s = \begin{bmatrix} k_x & 0 & 0 \\ 0 & k_y & 0 \\ 0 & 0 & k_z \end{bmatrix} \mathbf{d}_s, \quad (1)$$

where $\mathbf{f}_s \in \mathbb{R}^3$ denotes the external forces, \mathbf{K}_s denotes the stiffness matrix of the spring, and $\mathbf{d}_s \in \mathbb{R}^3$ is the displacement of the spring's end relative to its relaxed original position. In this paper, \mathbf{d}_s is equal to the target's current relative displacement to its initial state.

1) *Image-Based Target Pose Estimation*: In order to estimate the target pose, each marker needs to be tracked by the camera first. However, as the raw image captured by the

camera is full of noise, as seen in Fig. 2(b), markers cannot be detected robustly. Therefore, a bilateral filter and threshold are adopted to minimize the noise and preserve the boundary in images [27]. Then, markers are circled by a parameterized blob detection [28], as shown in Fig. 2(c). Finally, each marker's central pixel position ${}^I\mathbf{p}$ is returned.

The positions of markers ${}^M\mathbf{P} \in \mathbb{R}^{2 \times 12}$ in the target frame $\{M\}$ are known. The projection between the i -th marker centre ${}^M\mathbf{p}_i = [x_i, y_i]^T$ and its corresponding pixel ${}^I\mathbf{p}_i = [u_i, v_i]^T$ in the image frame $\{I\}$, as shown in Fig. 2(a), can be formulated as

$$\begin{aligned} {}^I\tilde{\mathbf{p}}_i &= \frac{1}{z} \begin{bmatrix} \frac{1}{\rho_w} & 0 & u_0 \\ 0 & \frac{1}{\rho_h} & v_0 \\ 0 & 0 & 1 \end{bmatrix} \begin{bmatrix} f & 0 & 0 & 0 \\ 0 & f & 0 & 0 \\ 0 & 0 & 1 & 0 \end{bmatrix} {}^C_M \mathbf{T} {}^M\tilde{\mathbf{p}}_i \\ &= \frac{1}{z} \underbrace{\begin{bmatrix} \frac{f}{\rho_w} & 0 & u_0 \\ 0 & \frac{f}{\rho_h} & v_0 \\ 0 & 0 & 1 \end{bmatrix}}_{\text{camera intrinsic } \mathbf{A}} \begin{bmatrix} r_{11} & r_{12} & t_x \\ r_{21} & r_{22} & t_y \\ r_{31} & r_{32} & t_z \end{bmatrix} \begin{bmatrix} x_i \\ y_i \\ 1 \end{bmatrix} \\ &= \frac{t_z}{z} \underbrace{\begin{bmatrix} h_{11} & h_{12} & h_{13} \\ h_{21} & h_{22} & h_{23} \\ h_{31} & h_{32} & 1 \end{bmatrix}}_{\text{homography } \mathbf{H}} \begin{bmatrix} x_i \\ y_i \\ 1 \end{bmatrix}, \quad (2) \end{aligned}$$

$$\text{where } {}^C_M \mathbf{T} = \begin{bmatrix} \mathbf{r}_1 & \mathbf{r}_2 & \mathbf{r}_3 & \mathbf{t} \\ 0 & 0 & 0 & 1 \end{bmatrix} = \begin{bmatrix} r_{11} & r_{12} & r_{13} & t_x \\ r_{21} & r_{22} & r_{23} & t_y \\ r_{31} & r_{32} & r_{33} & t_z \\ 0 & 0 & 0 & 1 \end{bmatrix} \text{ is}$$

the transformation from camera frame $\{C\}$ to marker frame $\{M\}$, ${}^M\tilde{\mathbf{p}}_i = [x_i, y_i, 0, 1]^T$ is the homogeneous form of ${}^M\mathbf{p}_i$, ${}^I\tilde{\mathbf{p}}_i = [u_i, v_i, 1]^T$ is the homogeneous form of ${}^I\mathbf{p}_i$, $i \in [0, n]$ ($n = 11$ for the prototype), f is the camera's focal length, ρ_w and ρ_h are the width and height of each pixel, respectively, $z = (h_{31}x_i + h_{32}y_i + 1)t_z$, and the camera intrinsic matrix \mathbf{A} is obtained via calibration with MATLAB camera toolbox [29].

According to the transformation relationship shown in Fig. 2(a), the current target pose related to its initial state ${}^{M_0}_{M_t} \mathbf{T}$ can be formulated as

$${}^{M_0}_{M_t} \mathbf{T} = ({}^{C}_{M_0} \mathbf{T})^{-1} {}^C_{M_t} \mathbf{T}. \quad (3)$$

The translation of ${}^{M_0}_{M_t} \mathbf{T}$ is equal to the displacement \mathbf{d}_s in (1). Then, the question becomes to get ${}^C_{M_0} \mathbf{T}$ and ${}^C_{M_t} \mathbf{T}$. The relationship between ${}^C_M \mathbf{T}$ and homography matrix \mathbf{H} can be formulated as

$$\begin{cases} \mathbf{r}_1 = t_z \mathbf{A}^{-1} [h_{11}, h_{21}, h_{31}]^T \\ \mathbf{r}_2 = t_z \mathbf{A}^{-1} [h_{12}, h_{22}, h_{32}]^T \\ \mathbf{t} = t_z \mathbf{A}^{-1} [h_{13}, h_{23}, h_{33}]^T \\ \mathbf{r}_3 = \mathbf{r}_1 \times \mathbf{r}_2 \end{cases}. \quad (4)$$

Because \mathbf{r}_1 is a unit vector, t_z can be calculated by $t_z = \frac{1}{\|\mathbf{A}^{-1} [h_{11}, h_{21}, h_{31}]^T\|}$. Therefore, to estimate ${}^C_{M_0} \mathbf{T}$ and ${}^C_{M_t} \mathbf{T}$, we only need to solve the homography matrix \mathbf{H}^0 and \mathbf{H}^t of the initial and current states.

Because each homography matrix \mathbf{H} has eight variables, at least four nonlinearly relative projections between ${}^M\mathbf{p}_i$ and

${}^I\mathbf{p}_i$ are needed to solve it, and each pair's relationship can be formulated as

$$\begin{bmatrix} {}^M p_{i,x} & 0 \\ {}^M p_{i,y} & 0 \\ 1 & 0 \\ 0 & {}^M p_{i,x} \\ 0 & {}^M p_{i,y} \\ 0 & 1 \\ -{}^M p_{i,x} {}^I p_{i,u} & -{}^M p_{i,x} {}^I p_{i,v} \\ -{}^M p_{i,y} {}^I p_{i,u} & -{}^M p_{i,y} {}^I p_{i,v} \end{bmatrix}^T \begin{bmatrix} h_{11} \\ h_{12} \\ h_{13} \\ h_{21} \\ h_{22} \\ h_{23} \\ h_{31} \\ h_{32} \end{bmatrix} = \begin{bmatrix} {}^I p_{i,u} \\ {}^I p_{i,v} \end{bmatrix}, \quad (5)$$

where $({}^M p_{i,x}, {}^M p_{i,y})$ and $({}^I p_{i,u}, {}^I p_{i,v})$ are coordinates of the i -th marker in the frame $\{M\}$ and its projection in the frame $\{I\}$. Based on this relationship and four pairs of projections, a set of equations can be established to solve \mathbf{H} . Substituting the solved \mathbf{H} into (4), ${}^C\mathbf{T}$ can be further obtained.

2) *Marker Image Registration*: Ideally, through substituting four detected ${}^I\mathbf{p}_i$ and their corresponding ${}^M\mathbf{p}_i$ into (5) we can calculate the homography matrix \mathbf{H} for each state. However, under external forces, the pose variation of the target causes the occlusion or halation of some markers and results in wrong correspondence between the image and the marker. As a result, the corresponding relationship between ${}^I\mathbf{p}_i$ and ${}^M\mathbf{p}_i$ changes over time, which invalidates the direct use of (5). Therefore, a registration process is required to label the currently detected markers' pixel positions ${}^I\mathbf{p}^t$ to their original indexes, as shown in Fig. 2(a), and we define this registered result as ${}^I\mathbf{p}^{t,r}$.

At the initial state $t = 0$, the target is installed perpendicularly to the optical axis. For the prototype we built, all the markers can be detected except the 11th marker (top marker) that is occluded by the channel, as shown in Fig. 2(b). Therefore, we define ${}^M\mathbf{P}^0$ by removing the 11th marker from ${}^M\mathbf{P}$ as the marker set at the initial state, and the projection \mathbf{H}^0 between ${}^M\mathbf{P}^0$ and ${}^I\mathbf{P}^0$ can be obtained according to (5). Substituting ${}^M\mathbf{p}_{11}$ and \mathbf{H}^0 back to (5), we can estimate ${}^I\mathbf{p}_{11}^0$. Then, the complete pixel-position array of the initial state ${}^I\mathbf{P}^{0,c}$ can be obtained by appending ${}^I\mathbf{p}_{11}^0$ to ${}^I\mathbf{P}^0$.

For the current state t , the pixel positions of the detected markers ${}^I\mathbf{P}^t \in \mathbb{R}^{2 \times m}$ (m is the number of detected markers, $m \leq n$) are returned by the blob detection. Nevertheless, these detected markers are directly labelled from bottom to top in the image. For example, the blob detection result of a random pose is shown in Fig. 2(d). Assuming ${}^I\mathbf{P}^{t-1,c}$ is known, we calculate the L1 norm of the distance vector between each ${}^I\mathbf{p}_i^t$ and ${}^I\mathbf{p}_j^{t-1,c}$, $i \in [1, m]$ and $j \in [1, n]$, and define it as e . The corresponding marker of ${}^I\mathbf{p}_i^t$ in ${}^I\mathbf{P}^{t-1,c}$ is the one that results in the minimal e , and its index is the desired j^* . Without loss of generality, the registration problem for the detected i -th hole is defined as

$$j^* = \arg \min_j \| {}^I\mathbf{p}_i^t - {}^I\mathbf{p}_j^{t-1,c} \|_1. \quad (6)$$

Repeating this registration for each detected marker ${}^I\mathbf{p}_i^t$ and updating ${}^I\mathbf{p}_{j^*}^{t,r} \leftarrow {}^I\mathbf{p}_i^t$, we can obtain ${}^I\mathbf{P}^{t,r}$ with the original indexes. We define the corresponding marker position set of ${}^I\mathbf{P}^{t,r}$ as ${}^M\mathbf{P}^t$. Substituting ${}^I\mathbf{P}^{t,r}$ and ${}^M\mathbf{P}^t$ to (5), the homography matrix of the current state \mathbf{H}^t can be calculated.

To ensure the image of the current state can be used as the reference for the next registration, i.e., the $t+1$ state, the

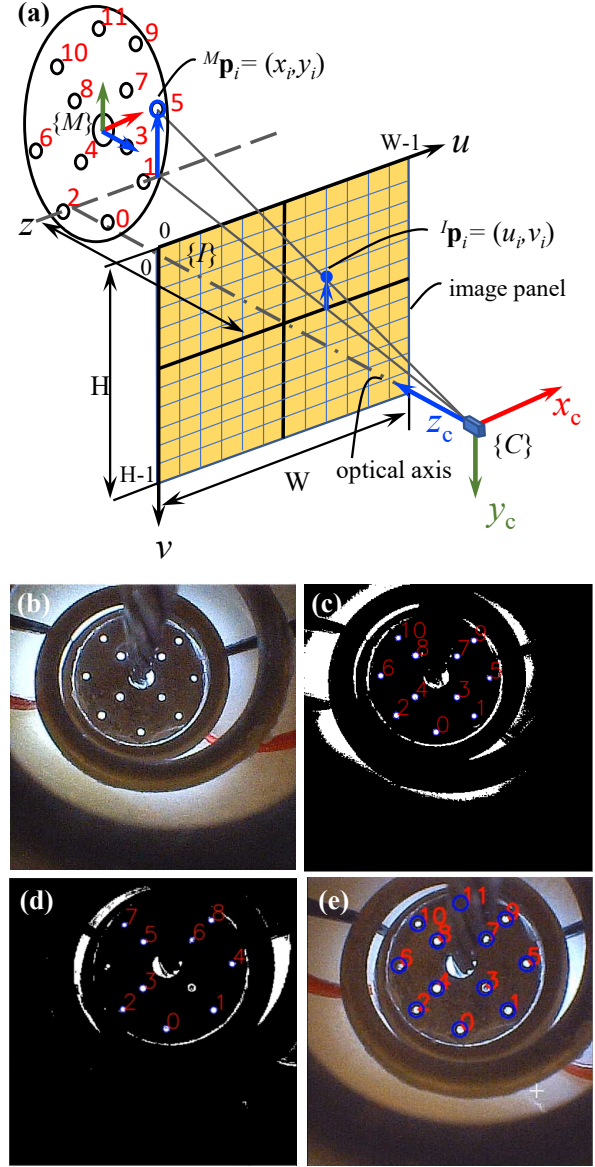


Fig. 2. (a) The projection relationship between the i -th marker (${}^M\mathbf{p}_i$) in the target frame $\{M\}$ and its corresponding pixel position (${}^I\mathbf{p}_i$) in image frame $\{I\}$. (a) also shows the original index of markers. (b) The directly captured image at the initial state. (c) The blob detected result at the initial state based on the filtered image. These detected marker centers are returned for pose estimation. (d) The blob detection result at a random pose, where the index of detected markers is different, and the points labelled with 3, 6 and 11 in the initial state are lost. (e) The registration result of (e), where markers were registered to their original indexes.

complete pixel-position set ${}^I\mathbf{P}^{t,c}$ of the current state also should be generated. By substituting undetected markers' coordinates in ${}^M\mathbf{P}$ and \mathbf{H}^t to (5), we can estimate their corresponding pixel positions ${}^I\mathbf{p}^{t,e}$. Then, ${}^I\mathbf{P}^{t,c}$ can be obtained by merging ${}^I\mathbf{p}^{t,e}$ with ${}^I\mathbf{P}^{t,r}$. For example, Fig. 2(e) shows the registration result and the generated complete image of Fig. 2(d).

3) *Felxure Deformation Estimation*: The transformation between the target and the camera at the initial state ${}^C_{M_0}\mathbf{T}$ can be calculated by substituting ${}^I\mathbf{P}^0$ and \mathbf{H}^0 into (4). Similarly, the transformation at the current state ${}^C_{M_t}\mathbf{T}$ can be obtained by substituting ${}^I\mathbf{P}^{t,r}$ and \mathbf{H}^t into (4). Then, the transformation

Algorithm 1 Pose and Force estimation of sensing module

Input: ${}^M\mathbf{P}$, \mathbf{A} , \mathbf{K}_s and *frame*
Output: ${}_{M_0}^M\mathbf{T}$, \mathbf{f}_s

- 1: set $t = 0$;
- 2: get ${}^I\mathbf{P}^t$ via blob detection based on *frame*;
- 3: get ${}^M\mathbf{P}^t$ by removing ${}^M\mathbf{p}_{n-1}$ from ${}^M\mathbf{P}$;
- 4: calc \mathbf{H}^t by substituting ${}^I\mathbf{P}^t$ and ${}^M\mathbf{P}^t$ to (5);
- 5: estimate ${}^I\mathbf{P}_{n-1}^0$ by substituting ${}^M\mathbf{p}_{n-1}$ and \mathbf{H}^0 to (5);
- 6: get ${}^I\mathbf{P}^{t,c}$ by appending ${}^I\mathbf{P}_{n-1}^0$ to ${}^I\mathbf{P}^t$;
- 7: calc ${}_{M_0}^C\mathbf{T}$ by substituting \mathbf{H}^t to (4);
- 8: **while** *frame do*
- 9: $t++$;
- 10: get ${}^I\mathbf{P}^t$ via blob detection based on *frame*;
- 11: **for** $i = 0; i < \text{col}({}^I\mathbf{P}^t); i++$ **do**;
- 12: $e' = \text{infinity}; j^* = \text{infinity};$
- 13: **for** $j = 0; j < \text{col}({}^I\mathbf{P}^{t-1,c}); j++$ **do**;
- 14: $e = \|{}^I\mathbf{p}_i^t - {}^I\mathbf{p}_j^{t-1,c}\|_1;$
- 15: **if** $e < e'$ **then**
- 16: $j^* = j; e' = e;$
- 17: **else**
- 18: $e' = e;$
- 19: **end if**
- 20: **end for**
- 21: **if** $j^* \leq \text{col}({}^I\mathbf{P}^{t-1,c})$ **then**
- 22: ${}^I\mathbf{p}_{j^*}^{t,r} \leftarrow {}^I\mathbf{p}_i^t;$
- 23: **end if**
- 24: **end for**
- 25: get corresponding ${}^M\mathbf{P}^t$ of ${}^I\mathbf{P}^{t,r}$ from ${}^M\mathbf{P}$;
- 26: calc \mathbf{H}^t by substituting ${}^I\mathbf{P}^{t,r}$ and ${}^M\mathbf{P}^t$ to (5);
- 27: get ${}^I\mathbf{P}^{t,e}$ by substituting ${}^M\mathbf{P}$ and \mathbf{H}^t to (2);
- 28: generate ${}^I\mathbf{P}^{t,c}$ by merging ${}^I\mathbf{P}^{t,r}$ with ${}^I\mathbf{P}^{t,e}$;
- 29: calc ${}_{M_0}^C\mathbf{T}$ by substituting \mathbf{H}^t to (4);
- 30: calc ${}_{M_t}^{M_0}\mathbf{T}$ by substituting ${}_{M_0}^C\mathbf{T}$ and ${}_{M_t}^C\mathbf{T}$ to (3);
- 31: calc \mathbf{f}_s by substituting ${}_{M_t}^{M_0}\mathbf{T}$ and \mathbf{K}_s to (1);
- 32: **end while**

${}_{M_t}^{M_0}\mathbf{T}$ can be calculated by substituting ${}_{M_0}^C\mathbf{T}$ and ${}_{M_t}^C\mathbf{T}$ into (3), which reflects the deformation of the flexure.

4) *Force Calculation*: The displacement of the spring \mathbf{d}_s is the translation vector of ${}_{M_t}^{M_0}\mathbf{T}$. Substituting \mathbf{d}_s and the spring's stiffness matrix \mathbf{K}_s into (1), we can estimate the external force \mathbf{f}_s . Ideally, the stiffness matrix \mathbf{K}_s represents the spring's characteristics that connect the camera and the target. However, this stiffness matrix \mathbf{K}_s should also consider the influence of wires and shelter, as they are parallel to the spring. In order to get the practical stiffness matrix \mathbf{K}_s , a calibration is carried out on the prototype and detailed in section III.

C. Haptics-Enabled Forceps and Force Estimation

1) *Micro-level Forceps Actuator*: To drive the forceps and conduct experimental verification, we designed a micro-level actuator, as shown in Fig. 1(d), which consists of upper and lower linear drivers that are responsible for grasping and pushing/pulling, respectively. The lower driver also compensates for the motion introduced by the flexure's deformation when the upper driver drives the forceps to grasp tissue.

The compensation is achieved by moving the lower driver's carrier for the same amount of the flexure's axial deformation estimated by the camera in the reverse direction. A commercial single-axis force sensor (ZNLBS-5kg, CHINO, China), with a resolution of 0.015N, is installed collinearly to the forceps and connected to the driving cable to measure the driving force.

2) *Pushing/Pulling Force Estimation (Mode-I)*: Integrating the sensing module into the forceps, we can enable its haptic sensing, and the haptics-enabled forceps are shown in Fig. 1(e). The base of the forceps is installed concentrically to the sensing module's head, and the driving cable passes through the reserved central channel. The cylindrical base connects the forceps to its carrying instrument (stainless tube). A prototype is also shown in the inset of Fig. 1(e), which has a 4mm diameter and 22mm total length and is used in the following description and experiments. The proposed haptics-enabled forceps can be easily integrated into a robotic surgical system with the micro-level actuator, such as the robot presented in Fig. 1(a). The forces applied to the forceps when they push or pull a tissue are also shown in Fig. 1(e). \mathbf{f}_p is the pushing/pulling force from the interactive tissue. \mathbf{f}_s is the elastic force from the spring, which can be directly estimated by (1). \mathbf{f}'_d is the driving force of the cable at the tool end. Ignoring friction, we assume $|\mathbf{f}'_d|$ equals $|\mathbf{f}_d|$ measured by the single-axis force sensor connected to the driving cable at the proximal side. Then, \mathbf{f}'_d can be formulated as $\mathbf{f}'_d = {}_{M_t}^{M_0}\mathbf{T}\mathbf{f}_d$. Finally, we can obtain the pushing/pulling force \mathbf{f}_p as

$$\mathbf{f}_p = -{}_{M_t}^{M_0}\mathbf{T}\mathbf{f}_d - \mathbf{f}_s. \quad (7)$$

For tissue touching, the contact force can also be estimated by (7) no matter if the forceps are closed or open.

3) *Grasping Force Estimation (Mode-II)*: The estimation of the grasping force is more challenging because it relates to the geometry and driving force applied to the forceps' cable, as depicted in Fig. 3. Although the sensing module can estimate the 3D elastic force \mathbf{f}_s and the orientation of \mathbf{f}'_d , we mainly consider the situation where the forceps grasp and pull tissue straightly as grasping is performed in the release condition.

The forces applied to the forceps when they grasp and pull a tissue are shown in Fig. 3(c). For convenience, we adopt F_- to denote the magnitude of force \mathbf{f}_- in the following sections. F_s is the elastic force from the spring and is directly estimated by (1). F_d is the driving force applied to the forceps' hinge and measured by the proximal single-axis force sensor. F_N and F_f are contact and friction forces from the grasped tissue, and we define the sum of the vertical components of F_N and F_f as the grasping force F_g , as shown in Fig. 3(c), and it can be formulated as

$$F_g = F_{N_1} \cos \frac{\theta}{2} + F_{f_1} \sin \frac{\theta}{2}, \quad (8)$$

where θ is the angle between the forceps' two jaws. According to the equilibrium equation on the grasped tissue, as depicted in the left inset of Fig. 3(c), the relationship between F_N , F_f , and external pulling force F_p can be formulated as

$$\begin{cases} F_p = (F_{f_1} + F_{f_2}) \cos \frac{\theta}{2} - (F_{N_1} + F_{N_2}) \sin \frac{\theta}{2} \\ F_{N_1} \cos \frac{\theta}{2} + F_{f_1} \sin \frac{\theta}{2} = F_{N_2} \cos \frac{\theta}{2} + F_{f_2} \sin \frac{\theta}{2} \end{cases}. \quad (9)$$

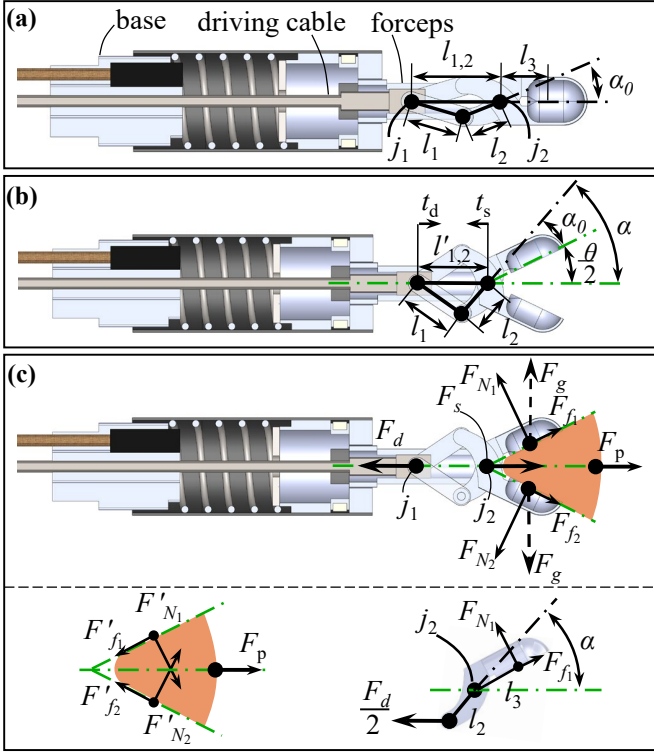


Fig. 3. (a) The sectional view of the haptics-enabled forceps when the two jaws are closed. (b) shows a state when the two jaws are open at θ . t_d is the movement of the driving cable, while t_s is the transformation of the sensing module's head estimated by the camera. (c) The forces applied to the forceps when they grasp and pull a tissue include driving force F_d from the cable, supporting force F_s from the sensing module, contact force F_N , and friction force F_f from the tissue. F_g denotes the grasping force that is equal to the sum of vertical components of F_N and F_f . The left inset shows the forces applied to the grasped tissue, where F_p is the pulling force from the tissue body, $F'_N = F_N$ and $F'_f = F_f$ are forces from the forceps. The right inset shows the forces that generate the momentum of one jaw about joint j_2 . F_d is measured by the proximal force sensor, while the driving distance t_d is measured by the upper driver's encoder of the micro-level actuator.

Since the momentum of one jaw about joint j_2 is zero, as plotted in the right inset of Fig. 3(c), we can further obtain the relationship between F_N and F_d as

$$F_{N_1} = \frac{F_d l_2 \sin \alpha}{2l_3}, \quad (10)$$

where $\alpha = \frac{\theta}{2} + \alpha_0$, the definitions of α , α_0 , l_2 and l_3 are shown in Fig. 3(b). θ and α_0 can be calculated based on the geometry relationship of the forceps' links. Fig. 3(a) shows the forceps' geometry at the initial state, i.e., the forceps are in the closed form, and the flexure is relaxed. According to the relationship of forceps' links at the initial state, we can get α_0 and formulate it as

$$\alpha_0 = \arccos \frac{l_1^2 - l_2^2 - l_{1,2}^2}{2l_1 l_{1,2}}, \quad (11)$$

where $l_{1,2}$ is the distance between forceps' two joints j_1 and j_2 . When the forceps are open at angle θ , the geometry changes to Fig. 3(b). At this stage, the angle α can be reformulated as

$$\alpha = \arccos \frac{l_1^2 - l_2^2 - l_{1,2}^2}{2l_1 l'_{1,2}}, \quad (12)$$

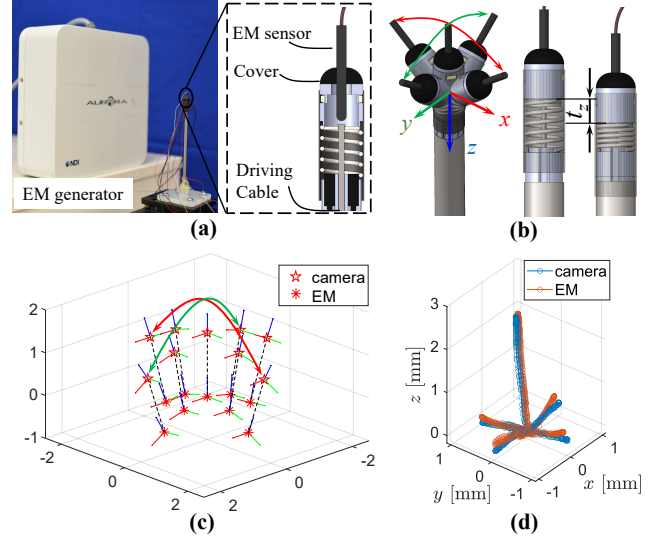


Fig. 4. (a) The experimental setup for evaluating pose estimation. The inset shows the configuration, where the EM tracking sensor was installed concentrically to the target. (b) The sensor's head was moved towards x , y and z directions during the experiments, and t_z denotes the transformation along z axis. (c) The orientation comparison between nine pairs of points that were estimated by the EM tracking system (*) and camera (*). (d) The position comparison between the continued EM tracking and camera estimation results.

TABLE I
ORIENTATION AND POSITION EVALUATION COMPARISON

Experiment	Average Deviation	Max Deviation
Orientation	0.056rad	0.147rad
Position	1.8233×10^{-6} mm	0.2265mm

where $l'_{1,2} = l_{1,2} - t_d + t_s$, t_d is the movement of the driving cable measured by the upper driver's encoder of the micro-level actuator, and t_s is the transformation of the sensor's head estimated by the sensing module. Then, we can get θ as

$$\theta = 2(\alpha - \alpha_0). \quad (13)$$

For a pair of forceps, we assume F_{N_1} equals F_{N_2} , and F_{f_1} equals F_{f_2} . Substituting (7), (9), (10), and (13) into (8) we obtain F_g and formulate it as

$$F_g = \frac{F_d l_2 \sin \alpha + F_p l_3 \sin(\alpha - \alpha_0)}{2l_3 \cos(\alpha - \alpha_0)}. \quad (14)$$

III. EXPERIMENTS

In this section, we first present the experiments on evaluating the method for target tracking and calibrating the stiffness matrix for external force estimation. Then, the evaluation of two modes of force estimation is described. Finally, groups of automatic robotic grasping procedures with the proposed system are illustrated as potential applications.

A. Evaluation of Target's Pose Estimation

1) *Experimental Setup*: Fig. 4(a) shows the experimental setup for pose estimation evaluation with an electromagnetic (EM) tracking system (Northern Digital Inc, Canada) with resolutions less than 0.1mm in position and 0.1° in orientation.

The EM tracking sensor was installed concentrically to the proposed force sensing module. During the experiment, the sensor's head was moved along x (red arrow), y (green arrow), and z (blue arrow) as indicated in Fig. 4(b).

2) *Pose Estimation Results*: The orientation comparison is based on nine pairs of samples distributed in the sensing module's workspace, as plotted in Fig. 4(c). Here, we use $(\alpha_{C,i}, \beta_{C,i}, \gamma_{C,i})$ and $(\alpha_{E,i}, \beta_{E,i}, \gamma_{E,i})$ to denote the pitch, roll, and yaw angles of camera estimation and EM tracking results of the i -th pair. The average and maximum deviations between EM tracking and our estimation result are calculated by $\max \frac{1}{n} (\sum_{i=1}^n \alpha_{C,i} - \alpha_{E,i}, \sum_{i=1}^n \beta_{C,i} - \beta_{E,i}, \sum_{i=1}^n \gamma_{C,i} - \gamma_{E,i})$ and $\max(\max_{i=1}^n (\alpha_{C,i} - \alpha_{E,i}), \max_{i=1}^n (\beta_{C,i} - \beta_{E,i}), \max_{i=1}^n (\gamma_{C,i} - \gamma_{E,i}))$, where $n = 9$. For position evaluation, the EM sensor and target were tracked continuously by the EM tracking system and camera, respectively, and the comparison is shown in Fig. 4(d). To calculate the average and max deviations between the EM and camera-tracking traces, we further calculated the average (d_a) and Hausdorff (d_h) distance by

$$\begin{cases} d_a = \max(\frac{1}{n} \sum_{i=1}^n d_{C_i,E}, \frac{1}{m} \sum_{j=1}^m d_{E_j,C}) \\ d_h = \max(\max_{i=1}^n (d_{C_i,E}), \max_{j=1}^m (d_{E_j,C})) \end{cases}, \quad (15)$$

where $d_{C_i,E} = \min_{j=1}^m (\|\mathbf{p}_{C,i} - \mathbf{p}_{E,j}\|_2)$, $\mathbf{p}_{C,i}$ and $\mathbf{p}_{E,j}$ denote positions of the camera estimation of point i and EM tracking of point j , $d_{E_j,C} = \min_{i=1}^n (\|\mathbf{p}_{E,j} - \mathbf{p}_{C,i}\|_2)$, $n=1336$ and $m=2181$ are the numbers of points recorded by the camera and EM tracking system, respectively. As listed in Table I, the average and maximum deviations of the orientation are 0.056rad and 0.147rad, and those of the position are 1.8×10^{-6} mm and 0.2265mm. This indicates the proposed method can track and estimate the target's pose reliably.

B. Stiffness Matrix Calibration and Verification

1) *Experimental Setup*: We used a series of weights to calibrate the haptics-enabled forceps' stiffness matrix. The calibration platform is shown in Fig. 5(a). Here, the micro-level actuator is used to adjust the position and hold the forceps. An orientation module is installed concentrically to the forceps for adjusting the direction of the pulling force provided by a cable. This cable is connected to the forceps' jaws, and the force F_w applied to it is adjusted by adding/removing weights.

2) *Calibration and Verification*: Two groups of data were collected for calibration and verification, respectively. When collecting the data for calibration in the x - y panel, as shown in Fig. 5(b), the orientation module made the cable align with the x and y axis, and the weight was increased from 0N to 0.49N at intervals of 0.07N. Then, for the z -axis direction, the driving force was increased from 0N to 5N at intervals of 0.5N. The target pose for each weight was recorded. Then, substituting the calibration data to (1), we obtained the stiffness matrix \mathbf{K}_s as

$$\mathbf{K}_s = \begin{bmatrix} 95.92 & 9.32 & -1.84 \\ 12.10 & 88.07 & -1.70 \\ 0.13 & 0.12 & 385.20 \end{bmatrix}.$$

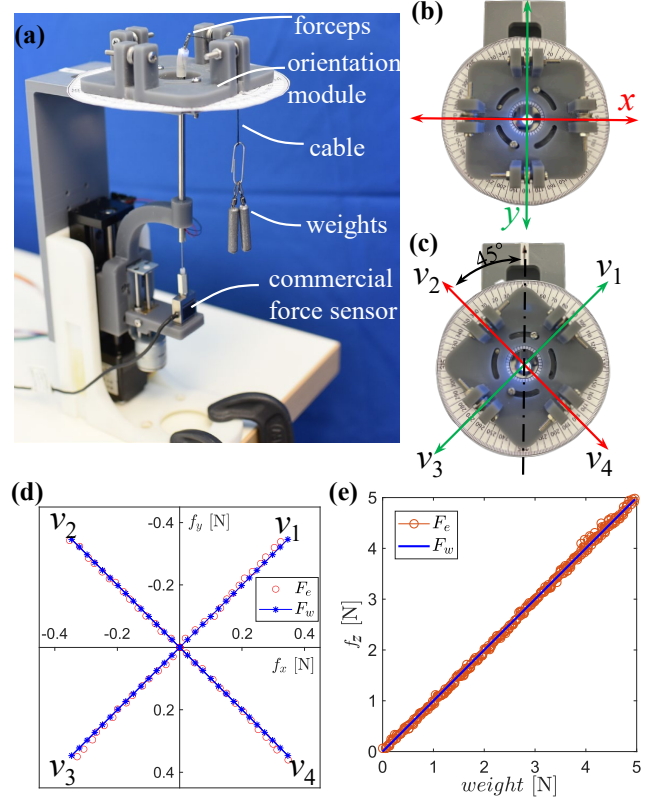


Fig. 5. (a) The experimental setup for stiffness matrix calibration. The forceps were pulled by a cable connected with changeable weights. The orientation module was used to adjust the pull direction of the forceps. (b) shows the setup for calibration data collection, where the orientation module was rotated 45° relative to that for calibration. v_1 , v_2 , v_3 , and v_4 indicate the pulling directions for verification in x - y panel. (d) and (e) show the verification results in x - y panel and z -axial direction, respectively. F_w and F_e denote the force generated by the weight and the estimated result.

To verify the calibrated \mathbf{K}_s , we rotated the orientation module for 45°, as shown in Fig. 5(c), and collected the data following the same procedure of calibration. For the x - y panel the interval was set to 0.035N, while for the z -axial direction the interval was 0.02N. The comparison of weights and estimated forces are plotted in Fig. 5(d) and (e), which show the results of the x - y panel and the z -axial direction, respectively. The average and maximum errors of (f_x, f_y, f_z) in these two comparison are (0.0009, 0.0013, 0.0105)N and (0.0177, 0.0154, 0.0995)N. This indicates the calibrated \mathbf{K}_s can be used to estimate the force applied to the forceps.

C. Evaluation of Mode-I: F_p Estimation

In this experiment, the grasped tissue was pulled in various directions by a cable connected to a force sensor. Fig. 6(a) shows that the grasped tissue is pulled from the initial state o_0 to $+y$ (o_1), $+x$ (o_2), $-y$ (o_3) and $-x$ (o_4). Snapshots show the states when the flexure has maximum deformation in different orientations, and the corresponding target positions are annotated below them. Fig. 6(b) shows the forces estimated by the proposed sensing module ($o_{e,i}$) and that measured by the commercial sensor ($o_{r,i}$) connected to the tissue-pulling cable. Table II lists the comparison result of F_p between $o_{e,i}$

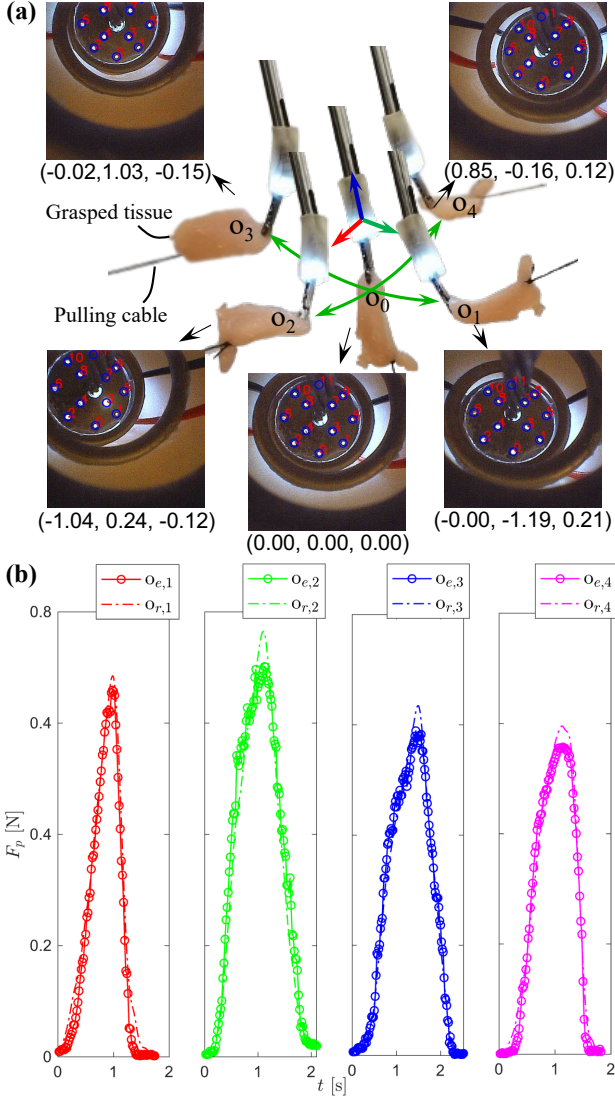


Fig. 6. The evaluation of Mode-I (F_p estimation) in various directions. (a) A grasped tissue was pulled by a cable from the initial state o_0 to $+y$ (o_1), $+x$ (o_2), $-y$ (o_3) and $-x$ (o_4). Snapshots show states when the flexure has maximum deformation in different orientations, with the corresponding target positions (in mm) annotated below them. (b) F_p estimated by our proposed sensing module ($o_{e,i}$) and that measured by the reference commercial sensor ($o_{r,i}$).

TABLE II
ERRORS OF F_p ESTIMATION IN VARIOUS ORIENTATION

Error	o_1	o_2	o_3	o_4
Average/N	0.0302	0.0380	0.0279	0.0233
Max/N	0.0766	0.1309	0.1281	0.0637

and $o_{r,i}$. The average and maximum errors of the four tests are under 0.02N and 0.14N, which indicates the forceps are valid for estimating F_p in various directions.

D. Evaluation of Mode-II: F_g Estimation

1) *Experimental Setup*: Fig. 7(a) shows the experimental setup, where a commercial pressure sensor (FlexiForce A201-1 lbs, Tekscan, USA), with a resolution of 0.02N, and a

force sensor (ZNLBS-5kg, CHINO, China) were adopted as references. The pressure sensor was grasped by the forceps for direct measurement of the grasping force. Because the pressure sensor's sensing area was a 10mm-diameter circle, 3D-printed surfaces were attached to the forceps' jaws to ensure sufficient contact. The driving force reached around 7N during the grasping action in each experiment. Since, from (14), we can see grasping force F_g is also related to pulling force F_p , we connected the pressure sensor to a commercial force sensor by a flexure to measure the pulling force applied to it.

2) *Evaluations*: We carried out three experiments with different θ configurations. Each experiment was presented as a continuous process, and the results are shown in Fig. 7(b), (c), and (d), where the subscript $i \in \{1, 2, 3\}$ denotes the i -th experiment that corresponds to $\theta = 10^\circ$, 30° , and 50° . The forceps grasped the pressure sensor and reached the target grasping force during 0~18s. After a pause phase (18~26s), the forceps pulled the grasped sensor backward for 25mm in the pulling phase (26~65s).

Fig. 7(b) depicts F_d provided by the driving cable and F_s measured by our proposed sensing module. F_s and F_d are almost equal in the grasping and pause phases. This is because the pulling force applied to the forceps was almost zero in these two phases, as there was no pulling action, and the pressure sensor was floating. On the contrary, in the pulling phase, F_d increases while F_s keeps constant. This is because the pressure sensor has been pulled, but the flexure deformation keeps constant. The difference between F_d and F_s is the pulling force F_p applied to the pressure sensor. As the three experiments followed the same procedure, their data almost overlay each other. However, because θ is configured differently, the time for performing the grasping is slightly different. The inset in Fig. 7(b) shows that the bigger θ is, the quicker the grasping finishes.

Fig. 7(c) shows the commercial sensor measured pulling force $F_{p,r,i}$ in the experimental procedure, and we compared it with forceps estimated result $F_{p,e,i}$. We can see that the pulling force of these three experiments almost overlay each other as the pulling distances are equal. A comparison between the commercial sensor results $F_{p,r}$ and our estimations $F_{p,e}$ is listed in Table III. The average and maximum errors of the three experiments are under 0.11N and 0.3N, respectively. This also reflects the forceps are valid for estimating the pulling force when they grasp tissue.

Fig. 7(d) compares the grasping force F_g , where $F_{g,e,i}$ and $F_{g,r,i}$ denote the forces of i -th experiment estimated by our proposed forceps and commercial pressure sensor, respectively. Because of the additional surfaces that are shown in the inlet of Fig. 7(a), l_3 in (14) was set as l^3 in these experiments. According to Fig. 7(d), we can see that when the driving force F_d is equal, the grasping force F_g is positively related to θ . This phenomenon conforms with the force calculation method (14). Table III lists the average and maximum errors between $F_{g,r}$ and $F_{g,e}$ of the three experiments, and they are under 0.03N and 0.11N, respectively. This indicates the forceps are valid for estimating the grasping force.

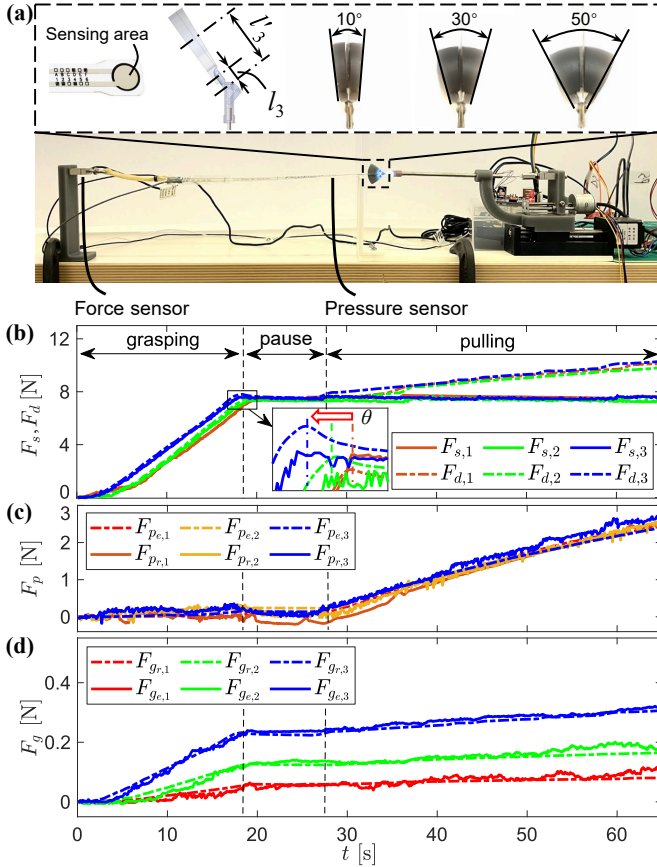


Fig. 7. The evaluation of Mode-II (F_g estimation). (a) The experimental setup, where a commercial pressure sensor and a force sensor were used as references for grasping and pulling forces, respectively. The inset shows three 3D-printed contact surfaces configured with $\theta = 10^\circ$, 30° and 50° . (b) shows F_d provided by the driving cable and F_s measured by our proposed force sensing module. Subscript $i \in (1,2,3)$ denotes the i -th experiment that correspond to $\theta = 10^\circ$, 30° and 50° . The inset shows that grasping time varies for different θ , and the red arrow shows the increased direction of θ . (c) The comparison of pulling force F_p , where $F_{pe,i}$ and $F_{pr,i}$ denote the forces of the i -th experiment estimated by our proposed sensing module and that measured by the commercial sensor, respectively. (d) The comparison of grasping force F_g , where $F_{ge,i}$ and $F_{gr,i}$ denote the forces of the i -th experiment estimated by our proposed sensing module and that measured by the reference commercial pressure sensor, respectively.

TABLE III
ERRORS OF F_g AND F_p ESTIMATIONS IN STRAIGHTLY GRASPING PROCEDURE

Force	Error	10°	30°	50°
F_p/N	Average	0.0898	0.0138	0.1144
	Max	0.2985	0.2782	0.1803
F_g/N	Average	9.7853×10^{-4}	0.0046	0.0049
	Max	0.0280	0.0298	0.0229

E. Ex vivo Robotic Experiments

1) *Experimental Setup*: To further verify the feasibility of the proposed system, we conducted a group of robotic experiments on an ex vivo tissue. Fig. 8 shows the experimental setup, where a UR-5 robotic arm was adopted as the macro-level actuator. The ex vivo chicken tissue was placed in a human body phantom to simulate the lesion, and the instrument was implemented through a simulated minimally

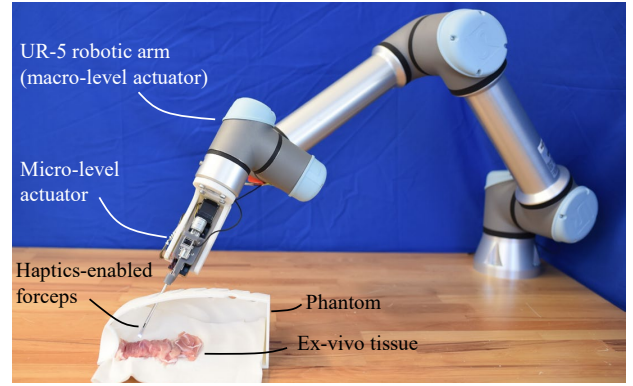


Fig. 8. The setup of robotic experiments. A 3D-printed human body phantom was used for placing ex vivo chicken tissue that simulated the lesion. The instrument was implemented through a simulated MIS port on the phantom.

invasive port on the phantom.

2) *Automatic Tissue Grasping*: We carried out automatic tissue grasping procedure with one targeted grasping force F_g^* and two different targeted pulling forces $F_p^{*,1}$ and $F_p^{*,2}$. The key experimental scenes and results are shown in Fig. 9, and the experiments can be roughly divided into five phases. Transformations between these phases were automatically performed depending on the grasping force F_g and pushing/pulling force F_p estimated by the haptics-enabled forceps.

With Mode-I enabled, the forceps were driven to touch the tissue during the touching phase (0~7.5s) until F_p reached the touching detection threshold $F_p^{*,t}$ followed by a short pending period (7.5~9.5s). Then, Mode-II was enabled, and the forceps performed the tissue grasping in the grasping phase (9.5~13.5s) until F_g reached the targeted value F_g^* . Finally, with another short pending period (13.5~15.5s), the grasped tissue was pulled up and held for a while with targeted pulling force F_p^* . Because the targeted pulling force F_p^* for the first and second group experiments were different, the time consumed for pulling varied. For the first group with $F_p^{*,1}=0.4N$, the period was around 6s, while for the second group with $F_p^{*,2}=0.2N$, it was around 2s.

Fig. 9(b) shows the measured driving force F_d and the estimated elastic force F_s of these experiments. Fig. 9(c) shows the estimated F_g , where $F_g^*=0.4N$ is the targeted grasping force for grasping action. Fig. 9(d) shows the estimated F_p , where $F_g^{*,t}=0.05N$ is the threshold for touch detection, while $F_p^{*,1}=0.4N$ and $F_p^{*,2}=0.2N$ are two target pulling forces for the first and second group experiments, respectively. According to the experiment results, we can see that the haptics-enabled forceps can be implemented in robotic surgery for multi-modal force sensing. With the proposed forceps, some surgical procedures can be performed automatically, and more information will be output for decision-making, i.e., it is potentially beneficial to task-autonomous robotic surgery.

IV. CONCLUSION

This paper presented a vision-based force sensing module that is adaptive to micro-sized biopsy forceps. An algorithm was designed to calculate the force applied to the sensing

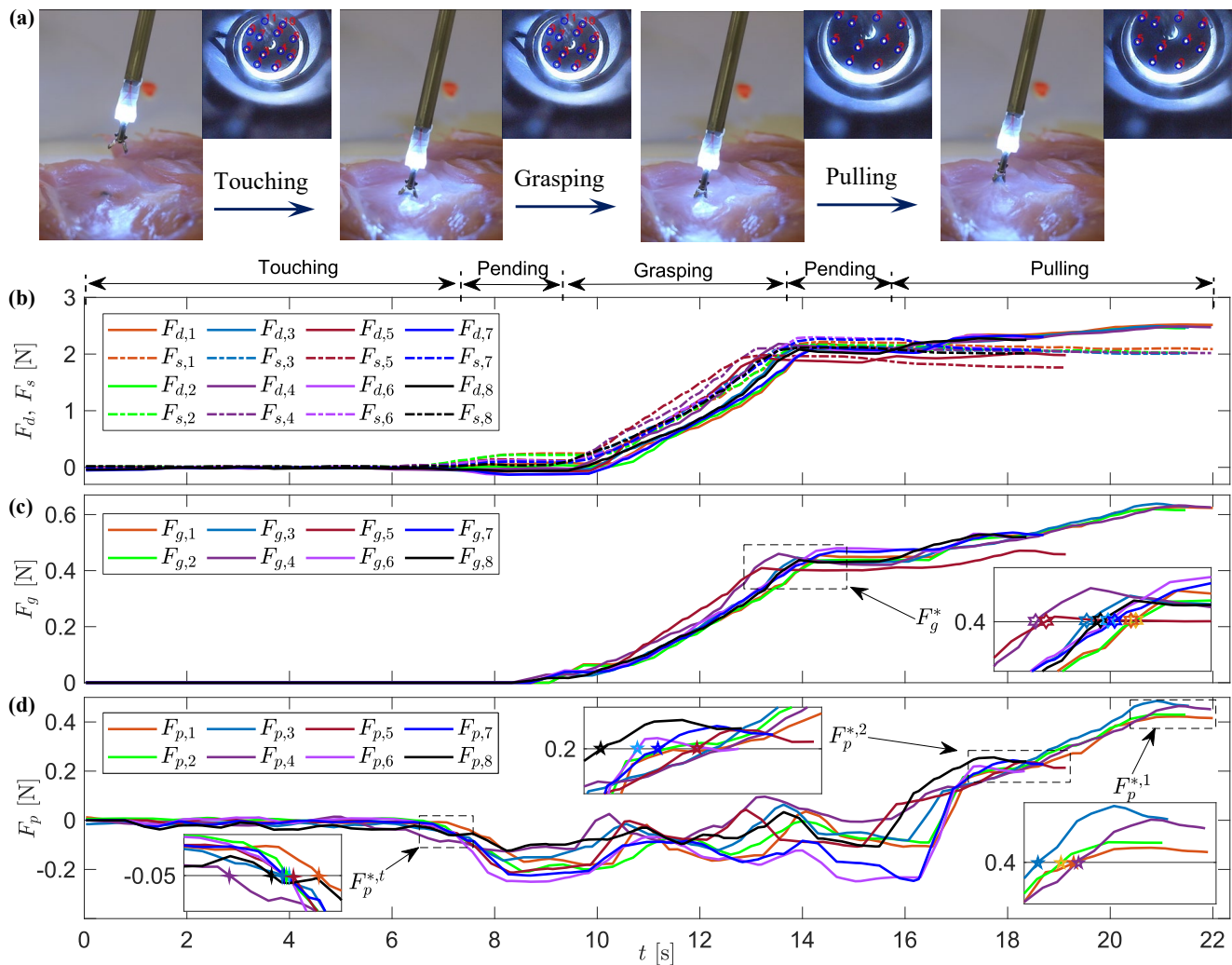


Fig. 9. The results of automatic tissue grasping experiments, where experiments can be classified into two groups with two different target grasping forces F_p^* . Experiments of the first group are marked with footnotes 1, 2, 3, and 4, while those of the second are marked with footnotes 5, 6, 7, and 8. (a) Key snapshots of the experimental procedure are attached with target tracking results. (b) shows the measured driving force F_d and the estimated elastic force F_s of these experiments. Plot (b) also shows the experimental phases. Touching means the forceps touch the targeted tissue in the opened form. Pending means the speeds of the system's motors have been set to zero for waiting. Grasping means the forceps grasp the touched tissue. Pulling means the forceps pull the grasped tissue. (c) shows the estimated F_g , where $F_g^*=0.4\text{N}$ is the targeted grasping force for grasping action. The partial enlargement shows each experiment has reached F_g^* successfully and is marked with a hexagon. (d) shows the estimated F_p , where $F_p^*=-0.05\text{N}$ is the threshold for touch detection, while $F_p^{*,1}=0.4\text{N}$ and $F_p^{*,2}=0.2\text{N}$ are two target pulling forces for the first and second group experiments, respectively. The left partial enlargement shows the touching detection and is marked with a four-pointed star for each experiment. The two right partial enlargements show the reaching of F_p^* of two group experiments and are marked with the pentagram.

module with a registration method for tracking and estimating the pose of the sensing module's target. Integrating the developed sensing module into the biopsy forceps, in conjunction with a single-axis force sensor at the proximal end, a haptics-enabled forceps was further proposed. Mathematical equations were derived to estimate the multi-modal force sensing of the haptics-enabled forceps, including pushing/pulling force (Mode-I) and grasping force (Mode-II). The methods for estimating multi-modal forces were presented with experimental verification. Groups of automatic robotic ex vivo tissue grasping procedures were conducted to further verify the feasibility of the proposed sensing method and forceps. The results show that the proposed method can be used for enabling multi-modal force sensing of the biopsy forceps, and the haptics-enabled forceps are potentially beneficial to automatic

tissue manipulation in applications such as thyroidectomy, ENT surgery, and laparoscopic surgery. The forceps will be integrated into a flexible robotic surgical system to further study the benefits of multi-modal force sensing for MIS.

REFERENCES

- [1] P. E. Dupont, B. J. Nelson, M. Goldfarb, B. Hannaford, A. Menciassi, M. K. O'Malley, N. Simaan, P. Valdastri, and G.-Z. Yang, "A decade retrospective of medical robotics research from 2010 to 2020," *Science Robotics*, vol. 6, no. 60, p. eabi8017, 2021.
- [2] P. E. Dupont, N. Simaan, H. Choset, and C. Rucker, "Continuum robots for medical interventions," *Proceedings of the IEEE*, vol. 110, no. 7, pp. 847–870, 2022.
- [3] L. Wu, F. Yu, T. N. Do, and J. Wang, "Camera frame misalignment in a teleoperated eye-in-hand robot: Effects and a simple correction method," *IEEE Transactions on Human-Machine Systems*, vol. 53, no. 1, pp. 2–12, 2022.

- [4] F. Feng, Y. Zhou, W. Hong, K. Li, and L. Xie, "Development and experiments of a continuum robotic system for transoral laryngeal surgery," *International Journal of Computer Assisted Radiology and Surgery*, vol. 17, no. 3, pp. 497–505, 2022.
- [5] Y. Cao, Z. Liu, H. Yu, W. Hong, and L. Xie, "Spatial shape sensing of a multisection continuum robot with integrated dtg sensor for maxillary sinus surgery," *IEEE/ASME Transactions on Mechatronics*, 2022.
- [6] R. V. Patel, S. F. Atashzar, and M. Tavakoli, "Haptic feedback and force-based teleoperation in surgical robotics," *Proceedings of the IEEE*, vol. 110, no. 7, pp. 1012–1027, 2022.
- [7] A. Talasaz, A. L. Trejos, and R. V. Patel, "The role of direct and visual force feedback in suturing using a 7-dof dual-arm teleoperated system," *IEEE transactions on haptics*, vol. 10, no. 2, pp. 276–287, 2016.
- [8] G.-Z. Yang, J. Cambias, K. Cleary, E. Daimler, J. Drake, P. E. Dupont, N. Hata, P. Kazanides, S. Martel, R. V. Patel *et al.*, "Medical robotics—regulatory, ethical, and legal considerations for increasing levels of autonomy," p. eaam8638, 2017.
- [9] A. Razjigaev, A. K. Pandey, D. Howard, J. Roberts, and L. Wu, "End-to-end design of bespoke, dexterous snake-like surgical robots: A case study with the raven ii," *IEEE Transactions on Robotics*, 2022.
- [10] J. Wang, J. Peine, and P. E. Dupont, "Eccentric tube robots as multiarmed steerable sheaths," *IEEE Transactions on Robotics*, vol. 38, no. 1, pp. 477–490, 2021.
- [11] A. Attanasio, B. Scaglioni, E. De Momi, P. Fiorini, and P. Valdastrì, "Autonomy in surgical robotics," *Annual Review of Control, Robotics, and Autonomous Systems*, vol. 4, pp. 651–679, 2021.
- [12] P. S. Zarrin, A. Escoto, R. Xu, R. V. Patel, M. D. Naish, and A. L. Trejos, "Development of a 2-dof sensorized surgical grasper for grasping and axial force measurements," *IEEE Sensors Journal*, vol. 18, no. 7, pp. 2816–2826, 2018.
- [13] W. Lai, L. Cao, J. Liu, S. C. Tjin, and S. J. Phee, "A three-axial force sensor based on fiber bragg gratings for surgical robots," *IEEE/ASME Transactions on Mechatronics*, vol. 27, no. 2, pp. 777–789, 2021.
- [14] A. Taghipour, A. N. Cheema, X. Gu, and F. Janabi-Sharifi, "Temperature independent triaxial force and torque sensor for minimally invasive interventions," *IEEE/ASME Transactions on Mechatronics*, vol. 25, no. 1, pp. 449–459, 2019.
- [15] U. Kim, Y. B. Kim, J. So, D.-Y. Seok, and H. R. Choi, "Sensorized surgical forceps for robotic-assisted minimally invasive surgery," *IEEE Transactions on Industrial Electronics*, vol. 65, no. 12, pp. 9604–9613, 2018.
- [16] F. Brinkmann, R. Hüttner, P. J. Mehner, K. Henkel, G. Paschew, M. Herzog, N. Martens, A. Richter, S. Hinz, J. Groß *et al.*, "Temperature profile and residual heat of monopolar laparoscopic and endoscopic dissection instruments," *Surgical Endoscopy*, pp. 1–11, 2021.
- [17] F. Gokcal and O. Y. Kudsı, "Robotic hiatal hernias and nissen fundoplication," *Robotic-Assisted Minimally Invasive Surgery: A Comprehensive Textbook*, pp. 37–46, 2019.
- [18] S. DiMaio, M. Hanuschik, and U. Kreaden, "The da vinci surgical system," in *Surgical robotics*. Springer, 2011, pp. 199–217.
- [19] R. Ouyang and R. Howe, "Low-cost fiducial-based 6-axis force-torque sensor," in *2020 IEEE International Conference on Robotics and Automation (ICRA)*. IEEE, 2020, pp. 1653–1659.
- [20] A. J. Fernandez, H. Weng, P. B. Umbanhowar, and K. M. Lynch, "Visiflex: A low-cost compliant tactile fingertip for force, torque, and contact sensing," *IEEE Robotics and Automation Letters*, vol. 6, no. 2, pp. 3009–3016, 2021.
- [21] G. Fagogenis, M. Mencattelli, Z. Machaidze, B. Rosa, K. Price, F. Wu, V. Weixler, M. Saeed, J. E. Mayer, and P. E. Dupont, "Autonomous robotic intracardiac catheter navigation using haptic vision," *Science robotics*, vol. 4, no. 29, p. eaaw1977, 2019.
- [22] M. A. Pucheta and A. Cardona, "Design of bistable compliant mechanisms using precision-position and rigid-body replacement methods," *Mechanism and Machine Theory*, vol. 45, no. 2, pp. 304–326, 2010.
- [23] J. Deng, K. Rorschach, E. Baker, C. Sun, and W. Chen, "Topology optimization and fabrication of low frequency vibration energy harvesting microdevices," *Smart Materials and Structures*, vol. 24, no. 2, p. 025005, 2014.
- [24] S. Keller and A. Gordon, "Equivalent stress and strain distribution in helical compression springs subjected to bending," *The Journal of Strain Analysis for Engineering Design*, vol. 46, no. 6, pp. 405–415, 2011.
- [25] A. K. Golahmadi, D. Z. Khan, G. P. Mylonas, and H. J. Marcus, "Tool-tissue forces in surgery: A systematic review," *Annals of Medicine and Surgery*, vol. 65, p. 102268, 2021.
- [26] A. Banach, F. King, F. Masaki, H. Tsukada, and N. Hata, "Visually navigated bronchoscopy using three cycle-consistent generative adver-

sarial network for depth estimation," *Medical image analysis*, vol. 73, p. 102164, 2021.

- [27] H. Singh, "Advanced image processing using opencv," in *Practical Machine Learning and Image Processing*. Springer, 2019, pp. 63–88.
- [28] A. Kaspers, "Blob detection," Master's thesis, 2011.
- [29] A. Fetić, D. Jurić, and D. Osmanković, "The procedure of a camera calibration using camera calibration toolbox for matlab," in *2012 Proceedings of the 35th International Convention MIPRO*. IEEE, 2012, pp. 1752–1757.



Tangyou Liu received the B.S. degree from the Southwest University of Science and Technology (SWUST) in 2017, Mianyang, China, and the M.S. degree as an outstanding graduate from the Harbin Institute of Technology, Shenzhen (HITSZ), Shenzhen, China, in 2021, supervised by Prof. Max Q.-H. Meng. Then, he worked in KUKA, China, in 2021, as a system development engineer and was awarded the champion of the KUKA China R&D Innovation Challenge. Now, he is pursuing his Ph.D. degree at the University of New South Wales (UNSW), Sydney, Australia, under the supervision of Dr. Liao Wu. His current research interests include medical and surgical robotics and human-robot interaction for minimally invasive surgery.



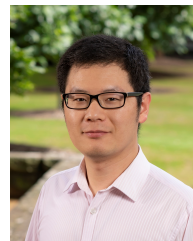
Tinghua Zhang received the B.S. and M.S. degrees in Mechanical Engineering from Jimei University (JMU) in 2020 and Harbin Institute of Technology (Shenzhen) (HITSZ) in 2023, respectively. He is working at The Chinese University of Hong Kong (CUHK) as a research assistant. His research interest is mainly in medical robotics, including robotic OCT, optical tracking and force sensing. He was awarded the best student paper finalist of IEEE ROBIO 2022.



Jay Katupitiya received his B.S. degree in Production Engineering from the University of Peradeniya, Sri Lanka and Ph.D degree from the Katholieke Universiteit Leuven, Belgium. He is currently an associate professor at the University of New South Wales in Sydney, Australia. His main research interest is the development of sophisticated control methodologies for the precision guidance of field vehicles on rough terrain at high speeds.



Jiaole Wang received the B.E. degree in mechanical engineering from Beijing Information Science and Technology University, Beijing, China, in 2007, the M.E. degree from the Department of Human and Artificial Intelligent Systems, University of Fukui, Fukui, Japan, in 2010, and the Ph.D. degree from the Department of Electronic Engineering, The Chinese University of Hong Kong (CUHK), Hong Kong, in 2016. He was a Research Fellow with the Pediatric Cardiac Bioengineering Laboratory, Department of Cardiovascular Surgery, Boston Children's Hospital and Harvard Medical School, Boston, MA, USA. He is currently an Associate Professor with the School of Mechanical Engineering and Automation, Harbin Institute of Technology, Shenzhen, China. His main research interests include medical and surgical robotics, image-guided surgery, human-robot interaction, and magnetic tracking and actuation for biomedical applications.



Liao Wu is a Senior Lecturer with the School of Mechanical and Manufacturing Engineering, University of New South Wales, Sydney, Australia. He received his B.S. and Ph.D. degrees in mechanical engineering from Tsinghua University, Beijing, China, in 2008 and 2013, respectively. From 2014 to 2015, he was a Research Fellow at the National University of Singapore. He then worked as a Vice-Chancellor's Research Fellow at the Queensland University of Technology, Brisbane, Australia from 2016 to 2018. Between 2016 and 2020, he was affiliated with the Australian Centre for Robotic Vision, an ARC Centre of Excellence. He has worked on applying Lie groups theory to robotics, kinematic modeling and calibration, etc. His current research focuses on medical robotics, including flexible robots and intelligent perception for minimally invasive surgery.